

We are IntechOpen, the world's leading publisher of Open Access books Built by scientists, for scientists

6,900

Open access books available

185,000

International authors and editors

200M

Downloads

Our authors are among the

154

Countries delivered to

TOP 1%

most cited scientists

12.2%

Contributors from top 500 universities



WEB OF SCIENCE™

Selection of our books indexed in the Book Citation Index
in Web of Science™ Core Collection (BKCI)

Interested in publishing with us?
Contact book.department@intechopen.com

Numbers displayed above are based on latest data collected.
For more information visit www.intechopen.com



Pattern Recognition in Medical Image Diagnosis

Noriyasu Homma
Cyberscience Center, Tohoku University
Japan

1. Introduction

Medical image diagnosis can be conducted through a highly intelligent cognitive process that requires special medical knowledge and experiences. It is not, of course, still completely clear what kind of information is needed and used for the highly intelligent diagnosis, but relatively low level features such as shapes, texture, and other pixel based statics extracted from the images can be used for the diagnosis. In this sense, medical images can be diagnosed, at least partially, by using pattern recognition algorithms. In this chapter, for lung cancer diagnosis by using X-ray computed tomography (CT) images, fundamentals and some advanced techniques of pattern recognition in medical image diagnosis will be studied extensively.

An early stage detection of the lung cancer is extremely important for survival rate and quality of life (QOL) of patients (Naruke et al., 1988). Although a periodical group medical examination is widely conducted by diagnosing chest X-ray images, such group examination is not often good enough to detect the lung cancer accurately and there is a high possibility that the cancer at an early stage cannot be detected by using only the chest X-ray images. To improve the detection rate for the cancer at early stages, X-ray CT has been used for a group medical examination as well (Iinuma et al., 1992; Yamamoto et al., 1993).

Using the X-ray CT, pulmonary nodules that are typical shadows of pathological changes of lung cancer (Prokop and Galanski, 2003) can be detected more clearly compared to the chest X-ray examination even if they are at early stages. This is an advantage of the X-ray CT diagnosis. In fact, it has been reported that the survival rate of the later ten years can reach 90% after the detection at early stages using X-ray CT images (I-ELCAP, 2006).

On the other hand, using the X-ray CT may exhaust radiologists because the CT generates a large number of images (at least over 30 images per patient) and they must diagnose all of them. The radiologists' exhaustion and physical tiredness might cause a wrong diagnosis especially for a group medical examination where most of CT images are healthy and only very few images involve the pathological changes. Therefore, some computer-aided diagnosis (CAD) systems have been developed to help their diagnosis work (Okumura et al., 1998; Lee et al., 1997; Yamamoto et al., 1994; Miwa et al., 1999).

Although these CAD systems can automatically detect pulmonary nodules with a high true positive rate (TP), the false positive rate (FP) is also high. To reduce the FP, several advanced methods such as neural network approaches have been proposed (Suzuki et al., 2003; Nakamura et al., 2005). However, there are still some fundamental problems such as a low

discrimination rate for variations of size and positional shift of nodule images. This is because they are still based on so-called low level or simple image recognition mechanisms with pixel oriented features compared to the radiologist's intelligent diagnosis process with more complex features.

In this chapter, to further reduce the FP, we propose new methods to extract and combine novel features from the CT images of pulmonary nodules (Homma et al., 2008). The extraction and combination of new features are motivated by the radiologist's higher level cognitive process in which several features are combined and integrated to conduct precise diagnosis. Simulation results demonstrate the effectiveness of the new features and the combination method for discriminating nodule shadows from non-nodule ones.

The rest of this chapter consists of as follows. Some filtering and feature extraction techniques will be introduced in section 2. To diagnose medical images, the region of interest (ROI) that is the target region of the recognition must be detected first and then some features can be extracted from the ROI for next step of the diagnosis. In section 3, for the extracted feature sets, the principal component analysis can be used to reduce the informational redundancy of the feature sets and to avoid unnecessary computational expensiveness of the classification algorithms. Then the effect of the extracted features on the nodule pattern classification will be evaluated by using the receiver operating characteristic (ROC) analysis. This evaluation will reveal what have been achieved and what cannot be achieved by the classification. To overcome the disadvantage of the classification algorithm, some advanced techniques will be developed in section 4. In section 5, concluding remarks including future perspective of this field will be given.

2. Filtering and Feature Extraction: Fundamentals for Lung Nodule Detection

In general, a discrimination method mainly consists of the feature extraction and pattern recognition techniques. The conventional image features are such as average, variance, and entropy of pixel values (Takizawa et al., 2001). However, they are not very effective and don't directly reflect target shapes in CT images that are one of the most important pieces of information used to discriminate between nodules and non-nodules. Therefore, we first pay attention to extracting a new shape feature that is more effective than conventional ones (Homma et al., 2008).

2.1 Detection of ROI: Morphological filters

First, we use the variable N-quoit filter (Okumura et al., 1998), based on a mathematical morphological technique (Haralick et al., 1987), to detect ROI from the original CT images. Let us consider an original image $I(x, y)$ of the pixel values at position (x, y) . To apply the N-quoit filter to the image I , we define two elemental functions, D with a disk domain K_D and R with a ring domain K_R , as follows (Nakayama et al., 1995).

$$D(x_1, y_1) = \begin{cases} 0, & (x_1, y_1) \in K_D \\ -\infty, & \text{otherwise} \end{cases} \quad (1)$$

$$R(x_1, y_1) = \begin{cases} 0, & (x_1, y_1) \in K_R \\ -\infty, & \text{otherwise} \end{cases} \quad (2)$$

where

$$K_D = \{(x_1, y_1) \mid x_1^2 + y_1^2 \leq r_1^2\} \quad (3)$$

$$K_R = \{(x_1, y_1) \mid r_1^2 \leq x_1^2 + y_1^2 \leq r_3^2\} \quad (4)$$

r_1 , r_2 , and r_3 are radii of the disk, internal, and external rings, respectively. Usually, $r_1 = r_3$ and $r_2 < r_3$.

The output of the N-quoit filter, q , is calculated as

$$q(x, y) = h_D(x, y) - h_R(x, y) \quad (5)$$

where h_D and h_R can be defined by using the operator \oplus of the Murkowski's set addition (Haralick et al., 1987)

$$\begin{aligned} h_D(x, y) &= I(x, y) \oplus D(x_1, y_1) \\ &= \max_{(x_1, y_1) \in K_D} \{I(x - x_1, y - y_1) + D(x_1, y_1)\} \end{aligned} \quad (6)$$

$$\begin{aligned} h_R(x, y) &= I(x, y) \oplus R(x_1, y_1) \\ &= \max_{(x_1, y_1) \in K_R} \{I(x - x_1, y - y_1) + R(x_1, y_1)\} \end{aligned} \quad (7)$$

Using the disk and ring functions, the output $q(x, y)$ results in large for island shadows in the image I , otherwise $q(x, y)$ becomes small. Since the pulmonary nodules often look like small islands in the CT slice images, the filter can effectively detect regions including nodule candidates with high q values.

2.2 Orientation features extraction

To extract features for nodules recognition, we binarize the original images I in the ROI as

$$I_\beta(x, y) = \begin{cases} 1, & I(x, y) \geq \text{mean}(I) + \beta \\ 0, & \text{otherwise} \end{cases} \quad (8)$$

and calculate three conventional features (mean, variance, and entropy of pixels intensity) of the binarized image I_β (Kondo et al., 2000).

Then, we apply a Gabor filter to the binarized image I_β and extract M orientation outputs.

The impulse response of the filter is defined as the harmonic function multiplied by the Gaussian function

$$g(x, y, \sigma, \lambda, \gamma, \theta) = \cos\left(2\pi \frac{x'}{\lambda}\right) \exp\left(-\frac{x'^2 + \gamma^2 y'^2}{2\sigma^2}\right) \quad (9)$$

where θ is the angle of orientation, σ is the bandwidth, γ is the aspect ratio, and λ is the wave length, respectively. x' and y' are given by

$$\begin{cases} x' = x \cos \theta + y \sin \theta \\ y' = -x \sin \theta + y \cos \theta \end{cases} \quad (10)$$

Orientation features are obtained from the convolution of image $I_\beta(x, y)$ and $g(x, y, \sigma, \lambda, \gamma, \theta)$ as

$$O(x, y) = I_\beta(x, y) * g(x, y, \sigma, \lambda, \gamma, \theta) \quad (11)$$

Fig. 1 shows examples of filtered images of four orientations. Using the new orientation features, the circle-like shadows can be discriminated from the other shapes. This is a

promising result because nodule shadows often look like circles. The orientation features involving such circle-shape information can thus be appropriate for the discrimination.

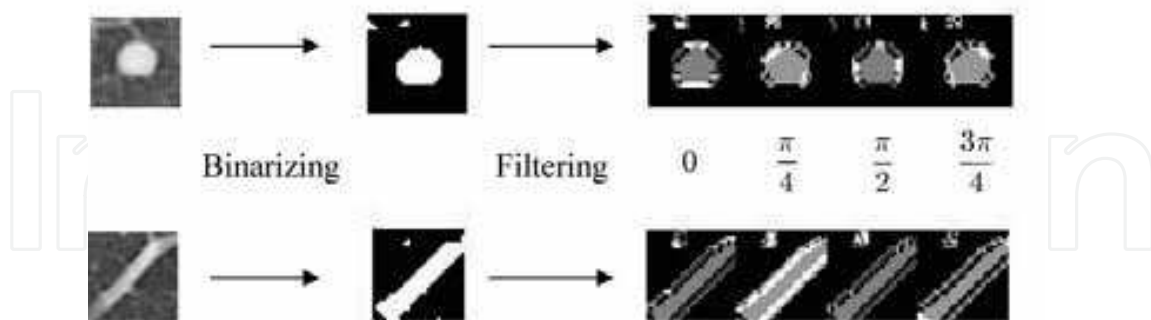


Fig. 1. Examples of four orientation filtered outputs.

For each orientation, we calculate the three features of mean, variance, and entropy of intensity. Consequently, we extract a total $3 \times (M + 1)$ features from the binarized image. Then we define a vector X of $3 \times (M + 1)$ features, $X = [x_1, x_2, \dots, x_{3(M+1)}]^T$, for the image in ROI. To eliminate the dimensional redundancy of the vector, we finally define a feature vector X' from the vector X by using the principal component analysis technique.

3. Nodule Pattern Classification

3.1 Pattern classification in principal component space

We make, respectively, P and Q clusters of nodules and non-nodules images of training data on the principal component feature space by K -means method. The numbers of nodule and non-nodule clusters, P and Q , can be determined automatically on the basis of variance equalization between clusters (Ngo et al., 2002). Then, we project test data X' into the feature space and calculate Euclidean distances between test data and all the cluster centers (Fig. 2). Here any other distances such as the inner product and Maharanobis distance can be used as the similarity measure, but if the variances are almost the same among clusters, then Maharanobis distance are equivalent to Euclidean distance.

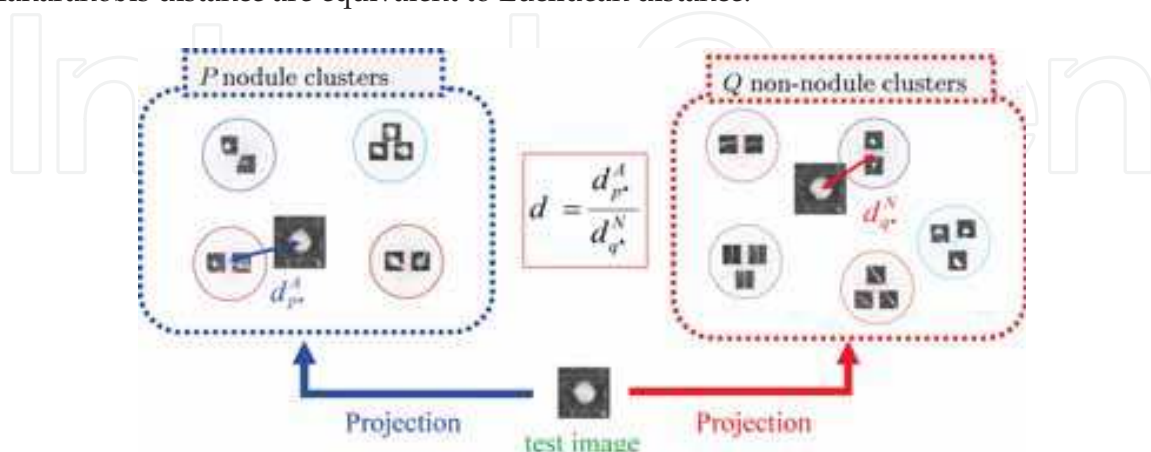


Fig. 2. Distances from the test image to centers of P nodule and Q non-nodule clusters.

Let us consider the $(P+Q)$ distances d_p^A , $p=1, 2, \dots, P$, from the P nodule clusters and d_q^N , $q=1, 2, \dots, Q$, from the Q non-nodule ones. The discrimination is conducted by comparing the minimum distances $d_{p^*}^A$, $p^* \in \{1, 2, \dots, P\}$, from the nearest nodule cluster and $d_{q^*}^N$, $q^* \in \{1, 2, \dots, Q\}$, from the non-nodule one. That is, if the ratio

$$d = \frac{d_{p^*}^A}{d_{q^*}^N} \quad (12)$$

is less than a threshold α , then the test image can be a nodule candidate; otherwise it is a non-nodule candidate.

3.2 Effect of orientation feature

To evaluate the effect of the orientation feature on the discrimination between nodule and non-nodule images, we have tested the proposed method by using a data set from the Web database of CT images (NICA, <https://imaging.nci.nih.gov/ncia/faces/baseDef.tiles>). We used a set of 297 nodule data images (208 training and 89 test images) and 1929 non-nodule data images (1351 training and 578 test images). The ROI size was 33×33 pixels and the binarizing threshold β was 40. The number of orientations M was 4 and the Gabor filter's parameters λ , σ , and γ were 1.5, 2.6, and 1, respectively. The number of principal components C was 5, defined as the minimum number that satisfies $\sum_{j=1}^C u_j > 0.95$ where u_j is the contribution ratio of principal component j . The number of clusters was 35 (25 nodules and 10 non-nodules).

3.2.1 Clustering results

Figs. 3 - 5 show sample images of feature vectors belonging to clusters made from training nodule images. The results demonstrate that each cluster consists of similar circle-like shapes of nodules. This suggests that the orientation features extracted from the nodule images can be useful for clustering them, and thus the proposed feature is effective for nodule discrimination.

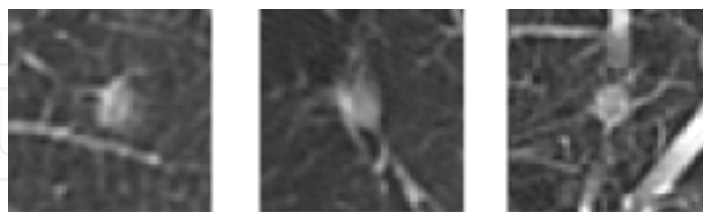


Fig. 3. Nodule images in cluster A. Images including relatively light and fuzzy boundary shadows are involved in this cluster.

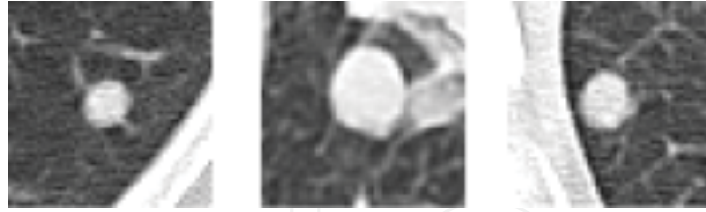


Fig. 4. Nodule images in cluster B. Images including relatively bright, smooth boundary and large circle shadows are involved in this cluster.

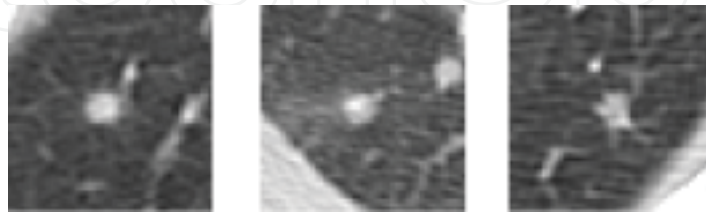


Fig. 5. Nodule images in cluster C. Images including small circle with spiculated boundary shadows are involved in this cluster.

On the other hand, Figs. 6 - 10 show sample images of feature vectors belonging to non-nodule clusters. The results demonstrate that some clusters are composed of similar shapes of non-nodules, but some are not. For example, in cluster nA (Fig. 6), most of images look like small circles, but there are a few images not involving such small circle shapes. Also, there are no similar shapes with each other in cluster nE (Fig. 10). This implies that non-nodule clusters are composed of various images with relatively large variance of feature vectors, compared to similar images with small variance of feature vectors in nodule clusters. Indeed, variances of feature vectors in non-nodule clusters are relatively large, while variances in nodule clusters are relatively small, although both variances were not large: The averages of the variances in non-nodule and nodule clusters were 0.003 and 0.001, respectively.

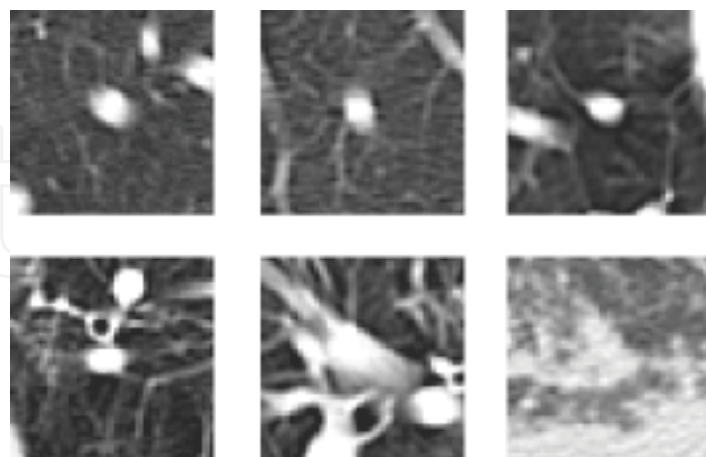


Fig. 6. Non-nodule images in cluster nA. Images including relatively small circle shadows are involved in this cluster.

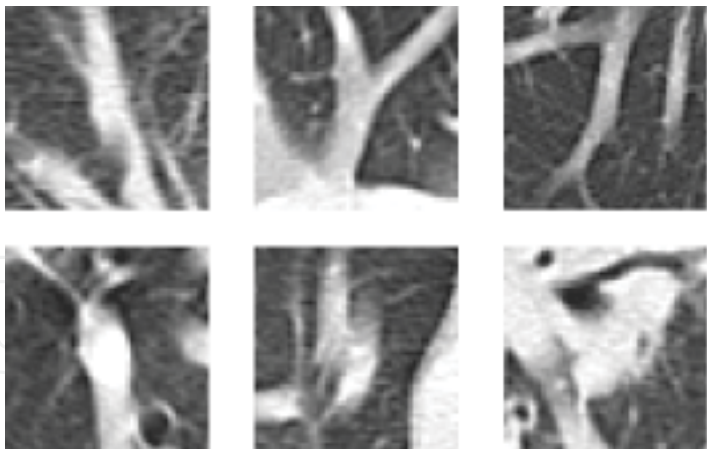


Fig. 7. Non-nodule images in cluster nB. Images including vertical line segments are involved in this cluster.

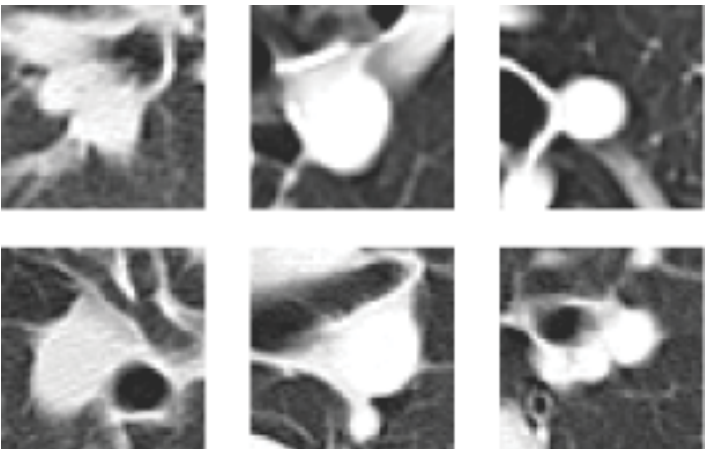


Fig. 8. Non-nodule images in cluster nC. Images including relatively large circle shadows are involved in this cluster.

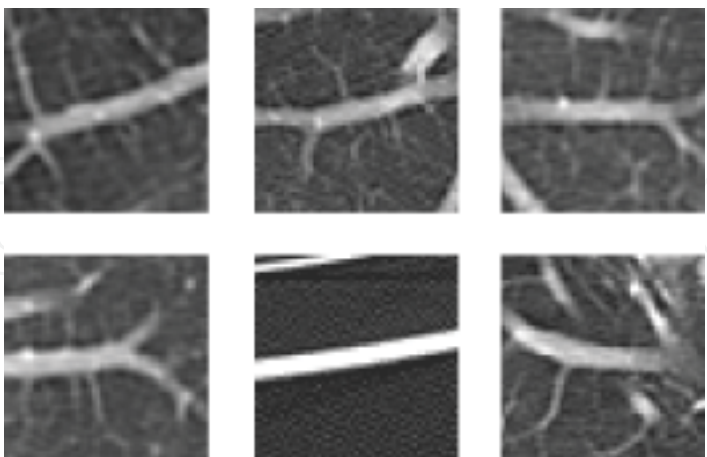


Fig. 9. Non-nodule images in cluster nD. Images including horizontal line segments are involved in this cluster.

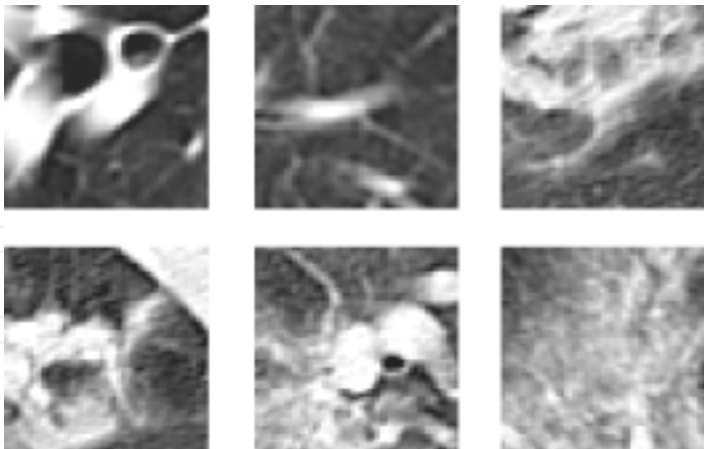


Fig. 10. Non-nodule images in cluster nE. Various shapes are involved in this cluster.

This suggests that further improvement for non-nodule clustering can be done by extracting more effective features from the original images. Such improvement will be discussed in section 4.2.

3.2.1 ROC analysis

Fig. 11 shows the 3 receiver operating characteristic (ROC) curves. Without 12 features of 4 orientations extracted by the Gabor filter, FP was about 80% when TP was 80%, while FP was about 35% by using the orientation features. The improvement of the discrimination rate (FP was improved from 80% to 35%) clearly demonstrates the effectiveness of the proposed feature on the diagnosis of pulmonary nodules. On the other hand, FP was about 30% under the same condition by using a massive training artificial neural network (MTANN) (Suzuki et al., 2003). Although these rates can be improved if we could choose more suitable settings for both the proposed and MTANN methods, we may claim that the discrimination performances of both methods are almost equivalent.

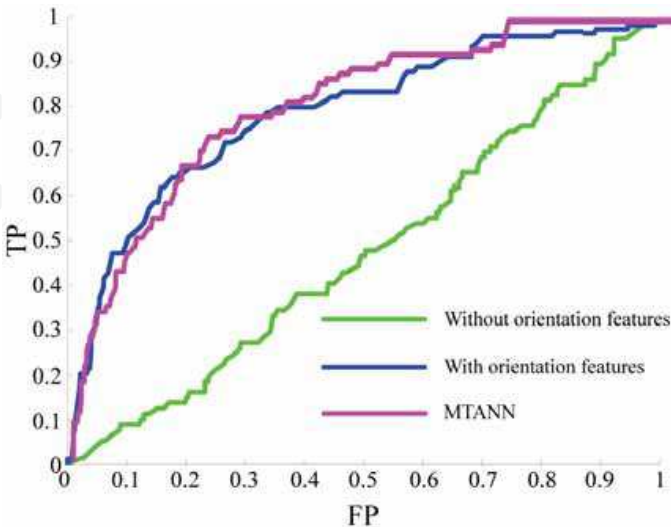


Fig. 11. ROC curves.

4. Advanced Methods for Lung Cancer Diagnosis

4.1 Variation feature along body axis

To further improve the discrimination rate for clinical use, we will now try to extract another effective feature (Homma et al., 2008). To begin with, let us consider why the discrimination performance using the orientation feature is not enough and what kind of images can be misjudged. For example, Fig. 12 shows a CT slice image of a patient. As mentioned in section 2.2, nodules often have circle-like shadows and thus we want to extract such shape information by using the Gabor filter. There are, however, some cases in which it is hard to discriminate between nodule and non-nodule images by using only such shape feature although the proposed one can be more effective than some conventional ones as demonstrated in the preceding section. Both images of nodules in cluster C (Fig. 5) and non-nodules in cluster nA (Fig. 6) have similar circle-like shapes, for example.

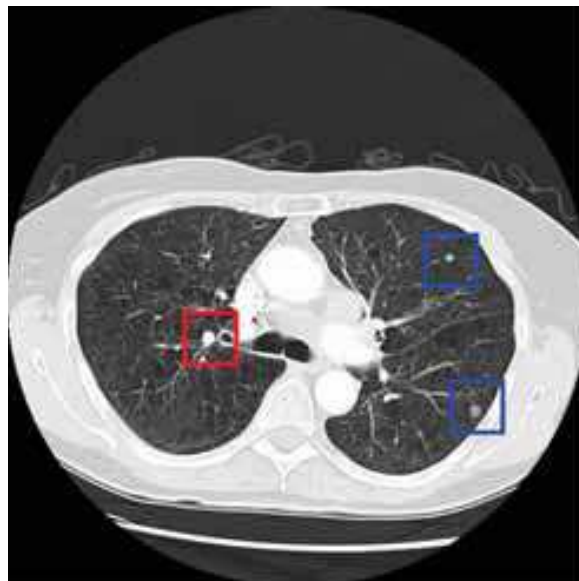


Fig. 12. ROI images detected by the variable N-quoit filter. Blue frames indicate images including nodules, whereas the red frame indicates a non-nodule image.

Different from the shape information within a CT slice, a novel feature can be extracted from shadow shapes across CT slices in the direction along the body axis (cranio-caudal direction). For example, Figs. 13 and 14 are CT slices above and below Fig. 12. Note that, according to a common opinion of several radiologists, circle-like shapes of non-nodules are almost shadows of blood vessels in the direction along the body axis. In this case, as seen in these figures, the blood vessels are cylinder-like shapes and thus the circle-like shadows remain at the same position if we look at slices above and below the target slice. On the other hand, nodules are often ball shapes. In this case, if we look at a slice above or below the target slice, the circle-like shadows often disappear. Thus, as a new feature, we employ the variation of CT values in the direction along body axis.

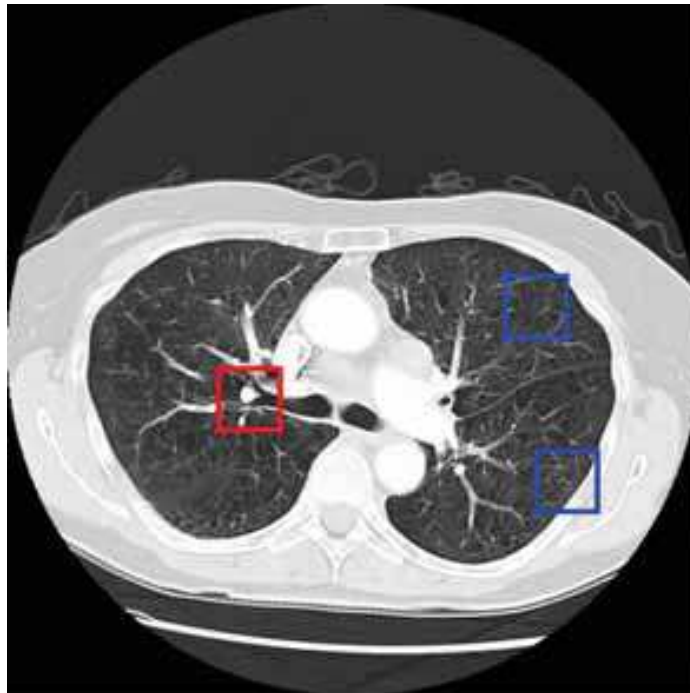


Fig. 13. CT slice image above the slice of Fig. 12. The red frame shows continuity between Figs. 12 and 13, in which a circle-like shadow remains at the same position in both figures. On the other hand, the blue frames show discontinuity that sizes and CT values of circle-like shadows in both figures are different from each other.

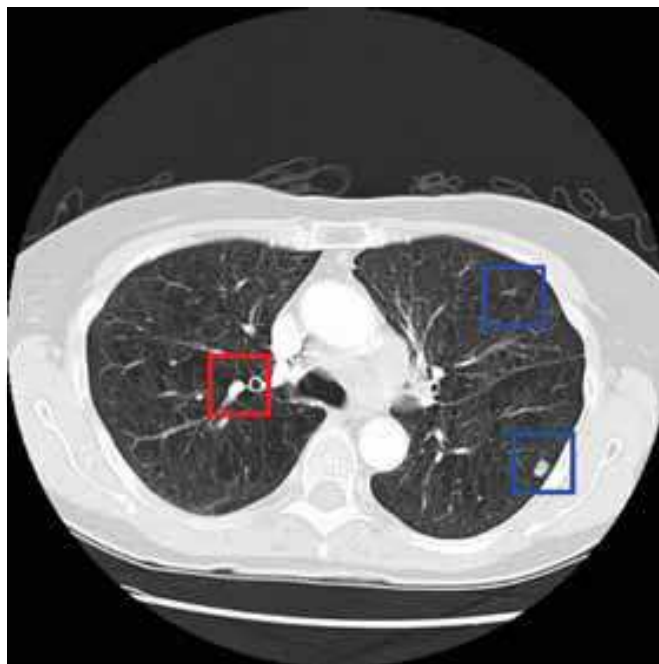


Fig. 14. CT slice image below the slice of Fig. 12. As same in Fig. 13, we can see continuity of a non-nodule shadow and discontinuity of nodule shadows.

To extract the variation feature, we first calculate the average pixel value of the shadow image in the ROI. If a shadow is of a non-nodule and a part of the cylinder-shape blood vessels along the body axis, continuity of the average values can be observed. On the other hand, if the shadow is of a nodule, then discontinuity of the average can be observed. In other words, for the non-nodule case, the average value is almost the same in above and below slices, while the average changes depended on the slices for the nodule case.

Let us denote the average values of the shadows V_m , V_u , and V_l for the target slice, and slices above and below the target, respectively. Using the averages, we define a new feature of shadow variation in the direction along the body axis T by

$$T = \max(T_u, T_l) \quad (13)$$

where

$$T_u = |1 - V_m / V_u| \quad (14)$$

$$T_l = |1 - V_m / V_l| \quad (15)$$

The concept of calculation of the feature extraction is illustrated in Fig. 15.

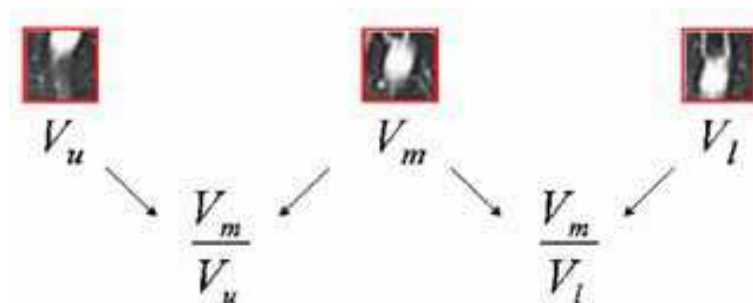


Fig. 15. Extraction of the shadow variation feature T .

The new feature T tends to be small for non-nodule shadows of the continuity case while it is large for nodule shadows of the discontinuity case. In fact, for the data used in section 3.2, the average value of the variation T for non-nodule images was 0.182, while the average of T was 0.479 for nodules.

4.1.1 Effect of variation feature

Here the shadow variation feature T was first applied to the ROI images and then more careful discrimination using the orientation features was conducted. That is, if the variation feature T of a candidate shadow in a ROI is less than a threshold T_h , the proposed method regards the shadow as a non-nodule. Otherwise, if $T \geq T_h$, the candidate shadow in the ROI is discriminated by using the orientation features as described in section 3.1. It might be worth mentioning an interesting fact that radiologists first detect ROIs of candidate shadows from the original CT slices by using such variation information along the body axis, and then diagnose the detected ROIs by using more detailed information such as shape, size, and CT values of shadows. This is the reason why we use the variation feature T before the orientation ones.

We have evaluated the effect of the new features on the discrimination rate by using the ROC analysis. Fig. 16 shows ROC curves by the conventional method and proposed methods without and with the variation feature T . By using the variation feature, FP was about 20% when TP was 90% in the case of the threshold $T_h = 0.206$. On the other hand, FP

was beyond 50% without the feature T . In other words, the discrimination rate FP was improved from about 50% to 20% under the condition TP=90%. Note that the condition TP=90% is good enough for clinical applications of pulmonary nodules diagnosis. Thus, the improvement clearly demonstrates usefulness of the variation feature.

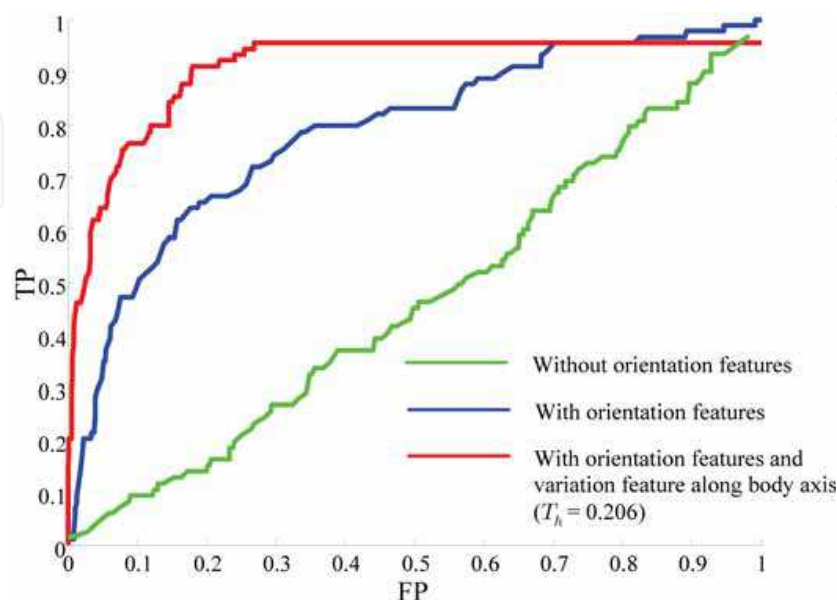


Fig. 16. ROC curves.

The fact that TP does not reach 100% in Fig. 16 might be a disadvantage of the proposed method with the variation T . This is because a few nodule shadows were regarded as non-nodule shadows by the variation threshold. As a second opinion for clinical use, however, robustness of the performance for various conditions is more important than TP=100% (TP \geq 90% is often good enough). Indeed, the performance is robust for various threshold values and thus it can be another advantage for clinical use.

In addition to this, as shown in Fig. 11, performance of MTANN (Suzuki et al., 2003) was almost the same as that of the proposed method without the variation feature. Consequently, performance of the proposed method with the variation feature can be superior to that of the MTANN. Also, similar information to the variation T can be obtained by 3-dimensional images reconstructed from helical CT data (Nakayama et al., 1995). However, calculation of the variation T is very simple and thus less computationally expensive.

4.2 Toward further improvement

4.2.1 A new feature of circle-like shapes

Fig. 17 shows examples of the true positive and false positive images under the condition $TP=90\%$ and $FP=20\%$. It seems that the TP and FP images can further be distinguished by their shapes: TP images are circle-like shapes while FP images are tree branch-like shapes of blood vessels or more complex shapes. The proposed orientation features do not work well for these images, although they are very effective for the greater part of images.



Fig. 17. Examples of the true positive and false positive images. True positive means that the discrimination result of the CAD system is nodule and it is really nodule whereas the false positive means that the system's result is nodule, but it is non-nodule.

As discussed in section 3.2.1, nodule images are clustered well compared to non-nodule images clustering. A wide non-nodule cluster region with high variances can affect the FP results because the distance to the FP image may be overestimated even if an image involved in a non-nodule cluster is close to the FP image in the feature vector space.

Another reason for this may be that the features are calculated for each orientation independently, but their relation among the orientations is not considered at least explicitly. For example, as illustrated in Fig. 18, we can expect that average pixel values extracted by the Gabor filter for all orientations are almost the same for circle-like shapes, while the averages are different from each other for line segments or tree branch shapes.

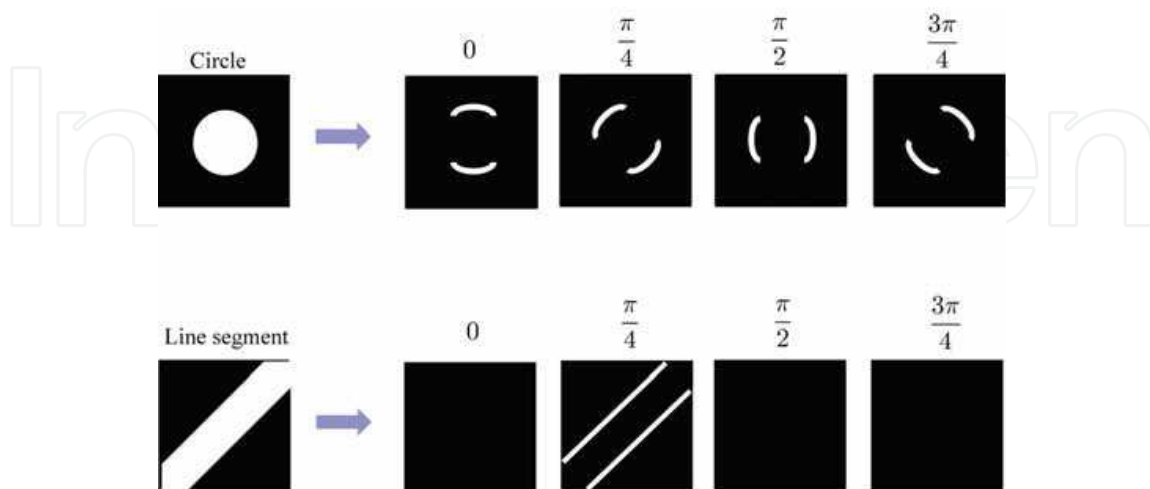


Fig. 18. Expected relation between different angles for circle-like and tree branch-like shapes.

To extract such differences between orientations, higher angle resolution may be necessary. However, as shown in Fig. 19, the discrete Gabor filter function is depended on the angle because of the small size of ROI. In such case, the sums of pixel values extracted the Gabor filter are different from each other even for the circle-like shapes.

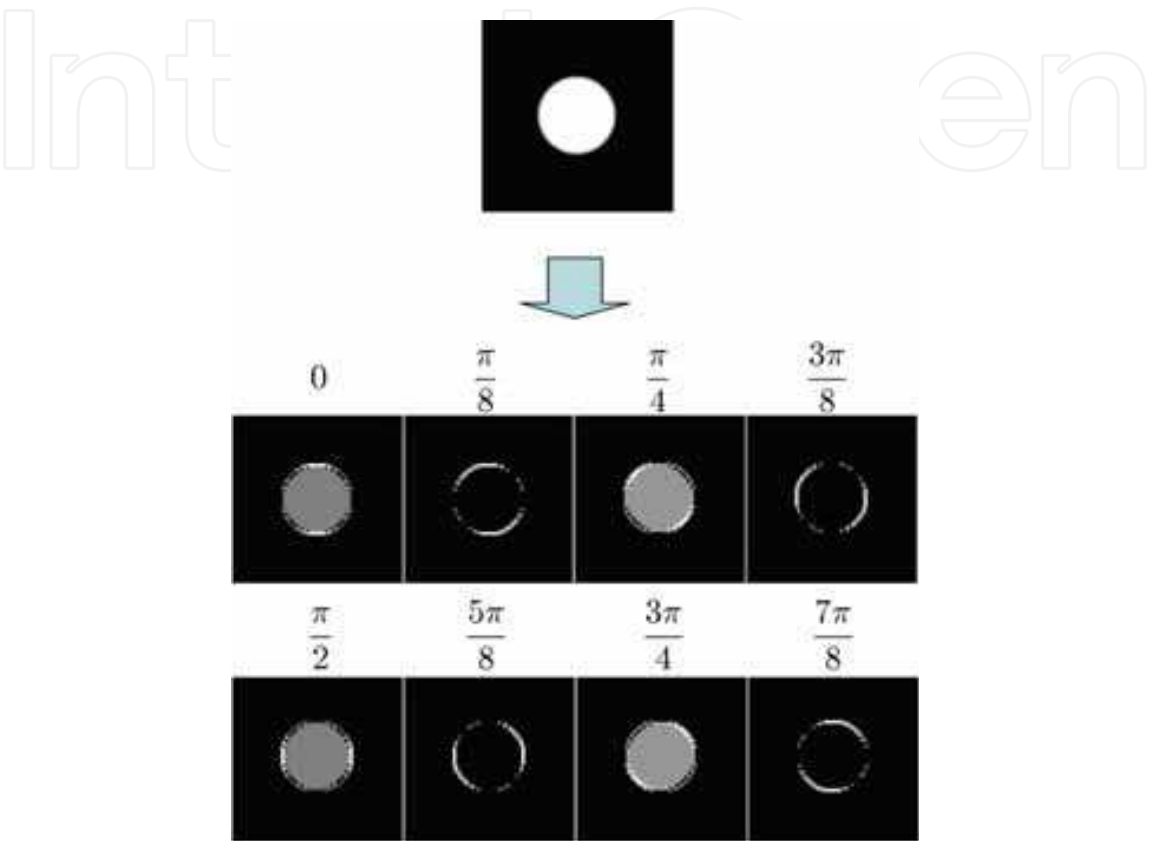
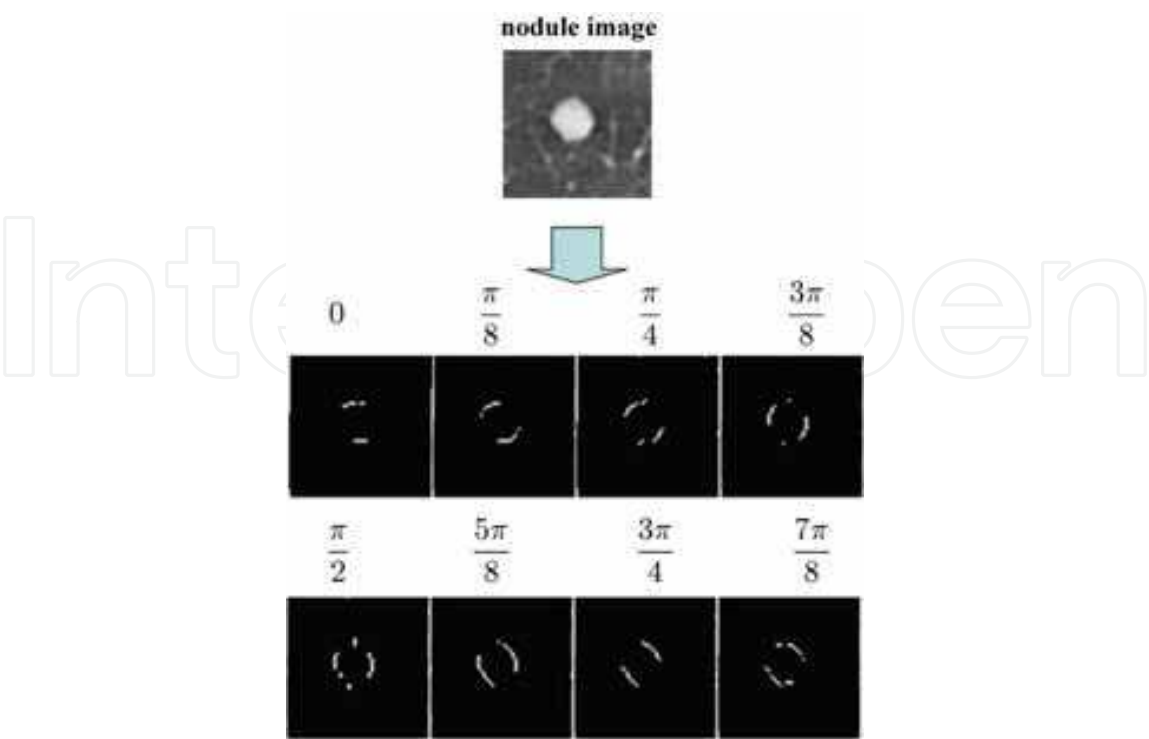
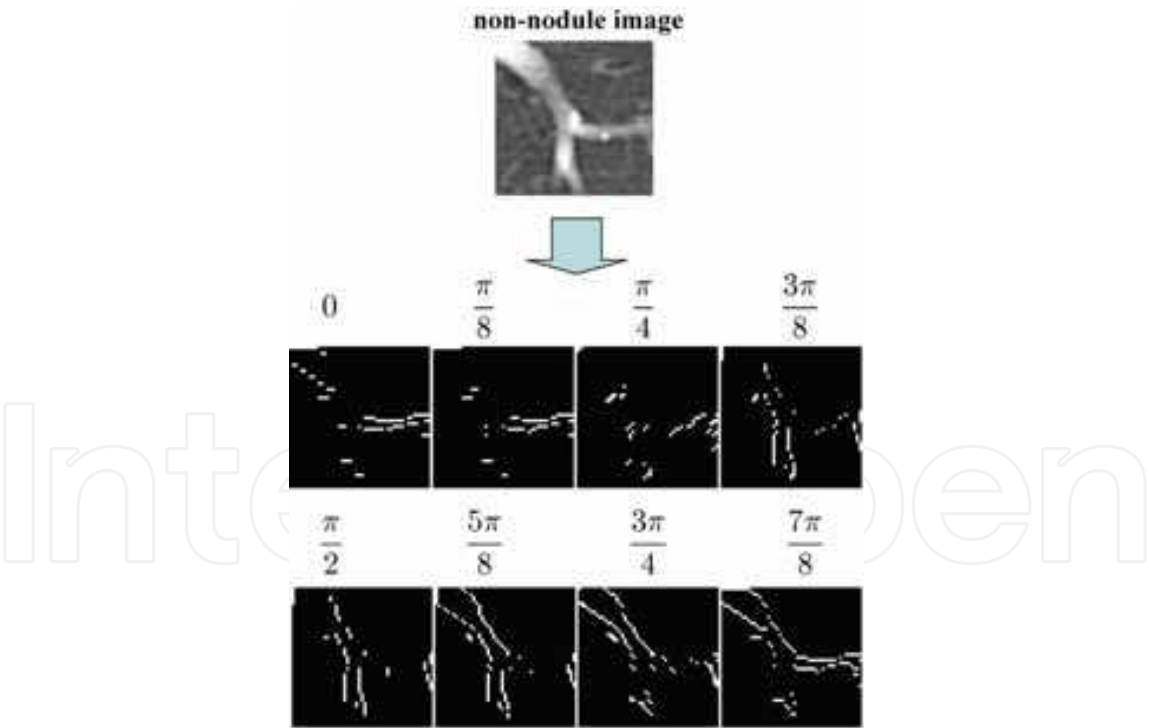


Fig. 19 Angle dependency of the Gabor filter outputs: Extracted values of inner and edge pixels are different from each other for various angles.

To overcome this problem, we conducted an edge detection technique as preprocessing the original images, and then the output images of the Gabor filter were binarized to eliminate the error caused by the spatial resolution (Homma et al., 2008). By this improvement, as shown in Fig. 20, average values of $M=8$ orientations can be almost the same for all orientations for the circle-like shape, while for the branch-like shapes, the 8 average values are different from each other depending on the orientation of the branches.



(a) Improved Gabor filter output for a circle-like shape.



(b) Improved Gabor filter output for a tree branch-like shape.

Fig. 20. Extracted values of inner and edge pixels are (a) almost the same for a circle-like shape, but (b) different from each other for a tree branch-like shape.

4.2.2 Improved results

Fig. 21 shows the standard deviation s of 8 average values for the TP and FP images. The numbers of TP and FP images were 72 and 76, respectively. Note that the standard deviations s for TP images are relatively small as expected for circle-like shapes, whereas the deviations for FP images are relatively large or widely distributed from large to small. Thus, after the discrimination by the variation along body axis and orientation features proposed in section 2, the TP and FP images can further be distinguished by the new feature s . In fact, FP=8% under the condition TP=90% when the algorithm classifies the images with $s > 0.01$ into non-nodules. In other words, FP decreased from 20% to 8% under the condition TP=90%.

Although the improvement achieved by the new feature is a good result, what we would like to stress here is that the combination of several effective features and classification techniques might be the most important for developing clinically useful CAD systems. The methods and the promising results presented in this chapter may support the importance of the combination.

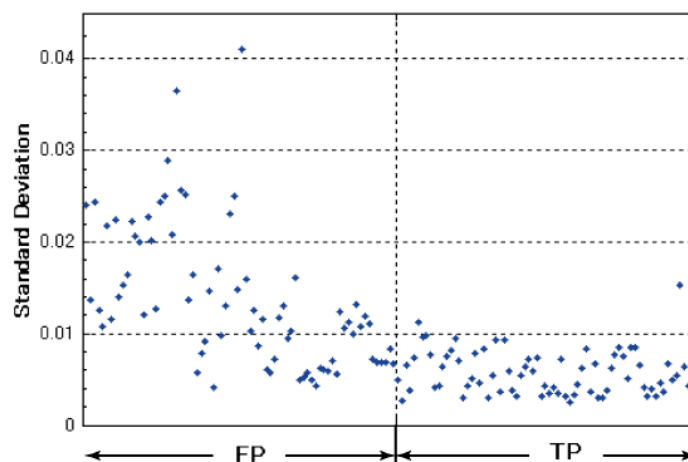


Fig. 21. The standard deviation s of M average values for TP and FP images. s for TP images are relatively small as expected for circle-like shapes.

5. Concluding Remarks

In this chapter, we have proposed a new method to detect pulmonary nodules in X-ray CT images. From results in this study, we may claim that the proposed orientation and variation features of nodules can be useful for the pulmonary nodule diagnosis. The proposed method is based on the radiologist's diagnosis process. That is, by using the variation feature of shadows in the direction along the body axis, the method first selects nodule candidates and then only for the candidates, instead of all the images, the method further discriminates nodules from non-nodules by using the orientation feature details of shadow shapes. The selection can thus contribute to less computational expense.

The methods introduced and developed in this chapter, however, aimed at only isolated circle-like shapes with the some morphological features, and thus non-isolated nodules (pathological changes) may not be detected by such methods. To improve the detection rate of such non-isolated nodules, Homma et al. have proposed a new technique that transforms

the non-isolated nodules connected to the walls of the chest into isolated ones (Homma et al., 2009). Again, we can combine the technique for non-isolated nodules with the methods for isolated nodules for clinical usefulness. The other drawbacks of the conventional methods can further be improved by incorporating some specific methods to solve the drawbacks.

6. References

- Haralick, RM. et al. (1987). Image Analysis Using Mathematical Morphology, *IEEE Trans. Pattern Analysis and Machine Intelligence*, Vol. 9, No. 4, pp. 532-550
- Homma, N., Takei, K., & Ishibashi, T. (2008). Combinatorial Effect of Various Features Extraction on Computer Aided Detection of Pulmonary Nodules in X-ray CT Images, *WSEAS Trans. Information Science and Applications*, Vol. 5, Issue 7, pp. 1127-1136
- Homma, N., Simoyama, S., Ishibashi, T., & Yoshizawa, M. (2009). Lung Area Extraction from X-ray CT Images for Computer-aided Diagnosis of Pulmonary Nodules by using Active Contour Model, *WSEAS Trans. Information Science and Applications*, Vol. 6, Issue 5, pp. 746-755
- Iinuma, T.; Tateno, Y., Matsumoto, T. et al. (1992). Preliminary specification of X-ray CT for lung cancer screening (LSCT) and its evaluation on risk-cost-effectiveness. *Nippon Acta Radiologica*, Vol. 52, pp. 182-190 (in Japanese)
- International Early Lung Cancer Action Program (I-ELCAP). (2006). Survival of Patients with Stage I Lung Cancer Detected on CT Screening, *New England J. Medicine*, Vol. 355, No. 17, pp. 1763-1771
- Kondo, M., Hirano, Y., Hasegawa, J., Toriwaki, J., Ohmatsu, H. & Eguchi, K. (2000). Classification of tumors in chest X-ray CT images into the solid and air-containing type and application to discrimination of the benign and malignant tumors, *TECHNICAL REPORT OF IEICE*, Vol. 100, No. 46, MI2000-16, pp. 27-32 (in Japanese)
- Lee, Y., Hara, T., Fujita, H., Itoh, S., & Ishigaki, T. (1997). Nodule detection on chest helical CT scans by using a genetic algorithm, *Proc. of IASTED International Conference on Intelligent Information Systems*, pp. 67-70
- Miwa, T., Kako, J., Yamamoto, S., Matsumoto, M., Tateno, Y., Iinuma, T., & Matsumoto, T. (1999). Automatic Detection of Lung Cancers in Chest CT Images by the Variable N-Quoit Filter, *Trans. Institute of Electronics, Information and Communication Engineers*, Vol. 82-D-II, pp. 178-187 (in Japanese)
- Nakamura, Y., Fukano, G., Takizawa, H., Mizuno, S., Yamamoto, S., Matsumoto, T., Sone, S., Takayama, F., Koyama, M., & Wada, S. (2005). Recognition of X-ray CT image using subspace method considering translation and rotation of pulmonary nodules, *TECHNICAL REPORT OF IEICE*, Vol. 104, No. 580, MI2004-102, pp. 119-124 (in Japanese)
- Nakayama, M., Tomita, T., Yamamoto, S. et al. (1995). Study of 3D Morphological Filtering Applied for Automatic Detection of Lung Cancer X-ray CT, *Medical Imaging Technology*, Vol. 13, No. 2, pp. 155-164 (in Japanese)
- Naruke, T., Goya, T., Tsuchiya, R. et al. (1988). Prognosis and survival in resected lung carcinoma based on the new international staging system. *J. Thorac Cardiovasc Surg*, Vol. 96, pp. 440-447

- National Cancer Imaging Archive (NCIA), <https://imaging.nci.nih.gov/ncia/faces/baseDef.tiles>
- Ngo, C. W., Pong, T. C., & Zhang, H. J. (2002). On clustering and retrieval of video shots through temporal slice analysis, *IEEE Trans. Mlt.*, Vol. 4, No. 4, pp. 446-458
- Okumura, T., Miwa, T., Kako, J., Yamamoto, S., Matsumoto, M., Tateno, Y., Iinuma, T., & Matsumoto, T. (1998). Variable-N-Quoit filter applied for automatic detection of lung cancer by X-ray CT, *Proc. of Computer-Assisted Radiology*, pp. 242-247 (in Japanese)
- Prokop, M. & Galanski, M. (2003). *Spiral and Multislice Computed Tomography of the Body*, Thieme Medical Publishers, Stuttgart
- Suzuki, K., Armato, S. G., Le, F., Sone, S. & Doi, K. (2003). Massive training artificial neural network (MTANN) for reduction of false-positives in computerized detection of lung nodules in lowdose computed tomography, *Med. Phys*, Vol. 30, No. 7, pp. 1602-1617
- Takizawa, H., Kamano, S., Yamamoto, S., et al. (2001). Quantitative analysis of cancer candidate regions in chest X-ray CT images, *J. Computer Aided Diagnosis of Medical Images*, Vol. 5, No. 2, pp. 4-11 (in Japanese)
- Yamamoto, S., Tanaka, I., Senda, M., Tateno, Y., Iinuma, T., Matsumoto, T., & Matsumoto, M. (1993). Image Processing for Computer Aided Diagnosis in the Lung Cancer Screening System by CT (LSCT), *Trans. Institute of Electronics, Information and Communication Engineers*, Vol. 76-D-2, pp. 250-260 (in Japanese)
- Yamamoto, S., Nakayama, M., Senda, M., Matsumoto, M., Tateno, Y., Iinuma, T., & Matsumoto, T. (1994). A Modified MIP Processing Method for Reducing the Lung Cancer X-ray CT Display Images, *Medical Imaging Technology*, Vol. 12, No. 6 (in Japanese)



Pattern Recognition

Edited by Peng-Yeng Yin

ISBN 978-953-307-014-8

Hard cover, 568 pages

Publisher InTech

Published online 01, October, 2009

Published in print edition October, 2009

For more than 40 years, pattern recognition approaches are continually improving and have been used in an increasing number of areas with great success. This book discloses recent advances and new ideas in approaches and applications for pattern recognition. The 30 chapters selected in this book cover the major topics in pattern recognition. These chapters propose state-of-the-art approaches and cutting-edge research results. I could not thank enough to the contributions of the authors. This book would not have been possible without their support.

How to reference

In order to correctly reference this scholarly work, feel free to copy and paste the following:

Noriyasu Homma (2009). Pattern Recognition in Medical Image Diagnosis, Pattern Recognition, Peng-Yeng Yin (Ed.), ISBN: 978-953-307-014-8, InTech, Available from: <http://www.intechopen.com/books/pattern-recognition/pattern-recognition-in-medical-image-diagnosis>

INTECH
open science | open minds

InTech Europe

University Campus STeP Ri
Slavka Krautzeka 83/A
51000 Rijeka, Croatia
Phone: +385 (51) 770 447
Fax: +385 (51) 686 166
www.intechopen.com

InTech China

Unit 405, Office Block, Hotel Equatorial Shanghai
No.65, Yan An Road (West), Shanghai, 200040, China
中国上海市延安西路65号上海国际贵都大饭店办公楼405单元
Phone: +86-21-62489820
Fax: +86-21-62489821

© 2009 The Author(s). Licensee IntechOpen. This chapter is distributed under the terms of the [Creative Commons Attribution-NonCommercial-ShareAlike-3.0 License](https://creativecommons.org/licenses/by-nc-sa/3.0/), which permits use, distribution and reproduction for non-commercial purposes, provided the original is properly cited and derivative works building on this content are distributed under the same license.

IntechOpen

IntechOpen